Supporting Information for

Upconversion Plasmonic Lasing from an Organolead Trihalide Perovskite Nanocrystal with Low Threshold

Yu-Jung Lu[1,2,3*], Teng Lam Shen[1,4], Kang-Ning Peng[1], Pi-Ju Cheng[1], Shu-Wei Chang[1], Ming-Yen Lu[5], Chih Wei Chu[1], Tzung-Fang Guo[4], and Harry A. Atwater[2*]

[1]*Research Center for Applied Sciences, Academia Sinica, Taipei 11529, Taiwan*

[2]*Thomas J. Watson Laboratories of Applied Physics, California Institute of Technology, Pasadena, California 91125, United States*

[3]*Department of Physics, National Taiwan University, Taipei 10617, Taiwan*

[4]*Department of Photonics, National Cheng Kung University, Tainan 701, Taiwan*

[5]*Department of Materials Science and Engineering, National Tsing-Hua University, Hsinchu 30013, Taiwan*

*To whom correspondence should be addressed.

*E-mail: yujunglu@gate.sinica.edu.tw(Y.J.L.), haa@caltech.edu (H.A.A.)

This PDF file includes:

Note S1. Characterization of plasmonic TiN films

Based on our previous work[1], the properties of the TiN film can be varied with the argon/nitrogen flow rate, target, DC/RF power, and growth temperature. We sputtered TiN film on silicon substrate with DC/RF magnetron sputtering at a chamber pressure of $< 6 \times 10^{-8}$ torr and at 800 °C. The detail growth parameters show in Table S1.

Table S1. Material properties and growth parameters of TiN films. We deposit thin TiN films via DC/RF sputtering. The properties of the TiN films are controlled by changing the growth parameter.

Epsilon near zero (ENZ) point (nm)	510 nm	670 nm
Ellipsometry fitting model	1 Drude and 2 Lorentz oscillators	1 Drude and 2 Lorentz oscillators
Target	TiN	Ti
Optical property	Plasmonic	Plasmonic
Film thickness (nm)	80	88
Substrate	Si	Si
Applied Power (W)	RF: 120 W	DC: 200 W
Ar/N$_2$ flow rate	12/0	1.5/18
Base Pressure (torr)	6×10^{-9}	6×10^{-8}
Gas pressure (mtorr)	3	5
Growth temperature (°C)	800	800

We measure the complex dielectric permittivity of the fabricated TiN films by using spectroscopic ellipsometry (J.A.Woollam Co.). We fit the ellipsometrically measured data by using the Drude-Lorentz model[2], which is a sum a Drude term and two Lorentz oscillators:

$$\tilde{\varepsilon}_{\mathrm{TiN}}(\omega) = \varepsilon_{\infty} - \frac{\omega_p^2}{\omega^2 - i\Gamma\omega} + \Sigma_{j=1}^2 \frac{f_j \times \omega_{oj}^2}{\omega_{oj}^2 - \omega^2 + i\gamma_j\omega}. \tag{S1}$$

We identify the values of the free parameters incorporated in the model by fitting them to the ellipsometry data. There are three free parameters in the Drude terms of Eq. (S1): the damping factor Γ_D, plasma frequency ω_p, and ε_{∞}. The plasma frequency relates to the electron effective mass m^* and the carrier density of the film N as follows: $\omega_p = \sqrt{\frac{Nq^2}{\varepsilon_0 m^*}}$. Here, q is the electron charge, ε_0 is the dielectric permittivity of vacuum. Each Lorentz oscillator in Eq. (S1) contains three fitting parameters: the oscillator strength f_j, the damping factor γ_j, and the oscillator position ω_{oj}. Here, the index j numerates the Lorentz oscillators (j=1,2,3). Table S2 summarizes the values of the obtained fitting parameters that have been used to produce Figure 2. In addition, the electrical properties of TiN films can be derived from the fitting parameters of the ellipsometry spectra presented in Table S2.

$$\text{Resistivity: } \rho\ (\mu\Omega\text{-cm}) = 1/(\varepsilon_0\ \omega_p^2\ \tau) \tag{S2}$$

$$\text{Collision frequency: } \tau\ (1/s) = \Gamma/\hbar \tag{S3}$$

The calculated electrical resistivity of TiN film is 21 $\mu\Omega$-cm, which is ten times larger than the reported resistivity of gold film (2.44 $\mu\Omega$-cm). Note that the conductivity σ is the reciprocal of the resistivity ρ. The results indicate that the ohmic loss of TiN film is less than that of gold.

Table S2. The Drude-Lorentz fitting parameters for the complex dielectric permittivity of two different TiN fims.

ENZ wavelength	ω_p (eV)	Γ_D (eV)	f_1	$\omega_{o,1}$ (eV)	γ_1 (eV)	f_2	$\omega_{o,2}$ (eV)	γ_2 (eV)	ε_∞
510 nm	6.9	0.5	4.8	5.5	3.1	0.4	2.5	2.1	1.4
670 nm	4.4	1.1	3.8	5.0	3.4	0.5	2.7	1.2	2.1

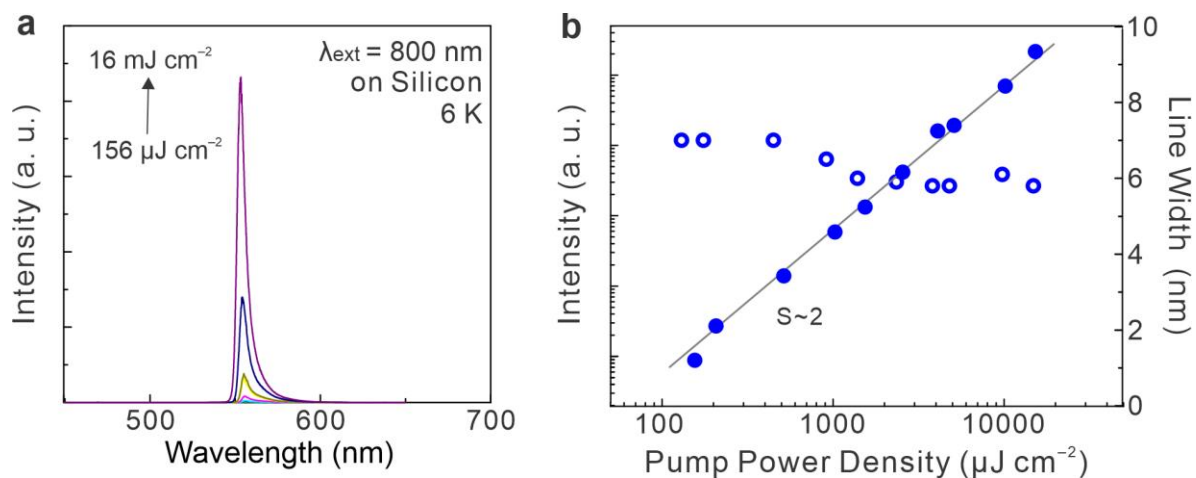## Note S2. Optical properties of perovskite nanocrystal

Figure S1. Power-dependent PL spectra recorded under two-photon excitations from a single MAPbBr$_3$ nanocrystal on silicon substrate measured at 6 K. (a) Power-dependent PL spectra. (b) A quadratic dependence of PL emission on the pump fluence of two-photon excitation, representing the feature of spontaneous emission. The line widths of PNC on silicon at various pump levels remain at approximately 6-7 nm.
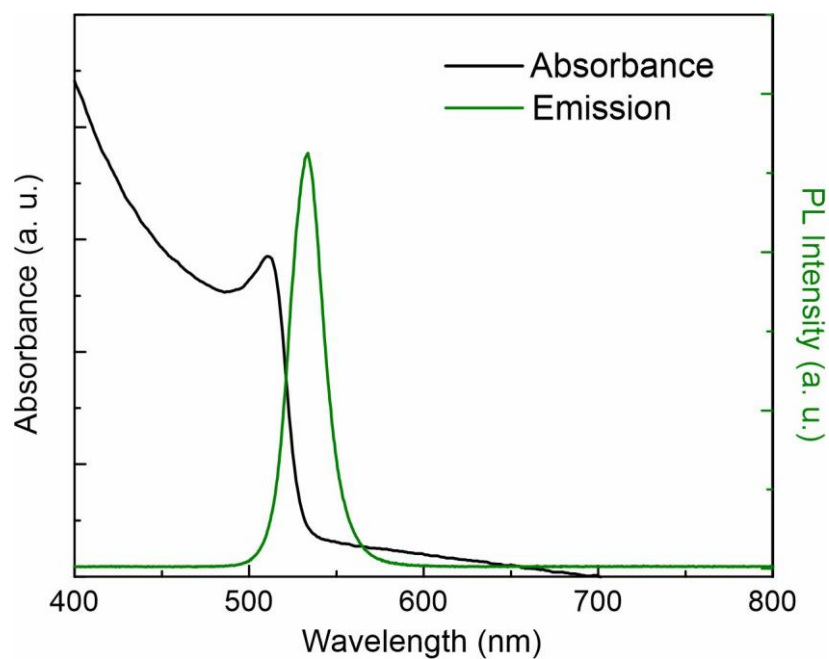
Figure S2. Optical characteristics of MAPbBr$_3$ nanocrystals film at room temperature. Optical absorption spectrum (black line) and photoluminescence spectrum (green line) of MAPbBr$_3$ Nanocrystals film. The perovskite nanocrystals with edge lengths in the range of 100 nm – 500 nm.
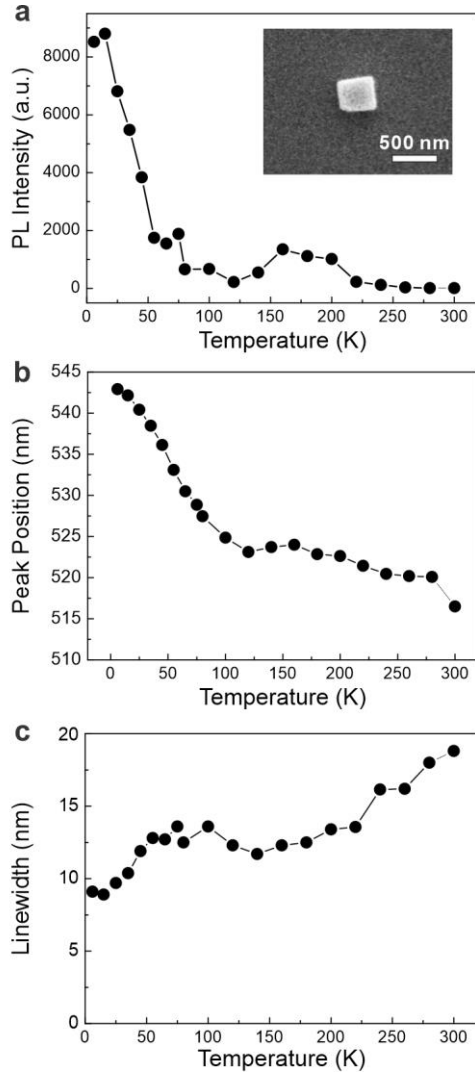
Figure S3. Temperature dependent photoluminescence (PL) of a single MAPbBr$_3$ nanocrystal on silicon substrate (pump fluence= 156 μJcm^{-2}). (a) The emission intensity as a function of temperature. (b) Position of the PL peaks as a function of temperature. (c) Linewidth of the PL peaks as a function of temperature.

Note S3. Table of the reported two-photon-pumped perovskite lasers.

Gain Material	Geometry	Dimension	Pump (pulsed width, repetition rate)	Temperature	Lasing Threshold
$CH_3NH_3PbBr_3$[3]	Microwire; Photonic mode	18.64 μm× 840 nm× 625 nm	100 fs, 1kHz	not mentioned	674 μJ/cm^2
$MAPbBr_3$[4]	Microwire and Microplate; Photonic mode	Microwire: 5.5 μm× 300 nm× 370 nm Microplate: 4 μm× 4 μm× 620 nm	150 fs, 1 kHz	not mentioned	Microwire: 112 μJ/cm^2 Microplate: 62 μJ/cm^2
$CsPbBr_3$[5]	Nanocrystal; Photonic mode	Microring: Inner diameter: 60 μm Thickness: 300 nm	90 fs, 1 kHz	Room temperature	0.8 mJ/cm^2
$CsPbBr_3$[6]	Nanorod; Photonic mode	Triangular cross-sections Leg: 250 nm, Base: 400 nm Length: 10 mm	80 fs, 1 kHz	Room temperature	0.60 mJ/cm^2
$CsPb_2Br_5$[7]	Microplate; Photonic mode	4.5 μm× 4.5 μm× 0.3–1.8 μm	100 fs, 1 kHz	Room temperature	21.5 mJ/cm^2
$CsPbBr_2Cl$[8]	Nanoplate; Photonic mode	1 μm× 1 μm× 150 nm	100 fs, 79 MHz	77 K	4.84 μJ/cm^2
$CsPbBr_3$[9]	Microrod; Photonic mode	33.96 μm× 5.622 μm× 3.494 μm	100 fs, 1 kHz	Room temperature	34.5 mJ/cm^2
$CsPbBr_3$[10]	Microsphere; Photonic mode	Diameter of 0.6–1.5 μm	40 fs, 10 kHz	Room temperature	203.7 μJ/cm^2
$CsPbI_3$[11]	Nanosheet; Photonic mode	10 μm× 10 μm× 6 nm	80 fs, 1 kHz	Room temperature	2.6 mJ/cm^2
$CsPbBr_3$[12]	Quantum Dots in silica sphere; Photonic mode	Diameter of 1–2 μm	35 fs, 1 kHz	Room temperature	430 μJ/cm^2
This Work $MAPbBr_3$	Nanocrystal; Plasmonic mode	300 nm× 300 nm× 100 nm	100 fs, 80 MHz	6 K	10 μJ/cm^2

Table S3. Lasing threshold of the reported upconversion perovskite lasers.

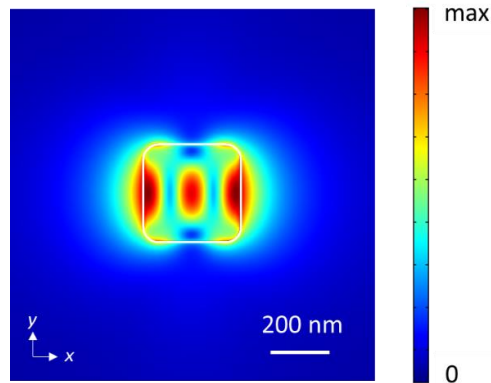## Note S4. Theoretical analysis of the lasing threshold.

Figure S4. Field profile of potential lasing mode at a wavelength of 551 nm on the middle plane of the oxide layer.

We solved the eigenmodes and corresponding frequencies of the plasmonic nanocavity inside the gain window of perovskite with the three-dimensional finite-element method (COMSOL eigenfrequency solver). In the model, the perovskite nanocrystal is placed on the three-layer structure composed of Al_2O_3, TiN, and Si. In the calculation, the refractive indices are 2.4^{13} for the perovskite, 1.68 for the oxide layer, and 4.09 for the silicon substrate. The index of TiN is extracted from the ellipsometry data. Only two modes with adequate quality factors and well-confined modal profiles were found. The one with the longer photon lifetime is the Fabry-Perot-like mode, whose modal profile $|\mathbf{E}|$ on the middle plane of Al_2O_3 is shown in Figure S4. This modal profile exhibits strong confinement at the wavelength of 551 nm. A very small modal volume of a confined mode ($\sim 0.06 \lambda^3$) is calculated by the three-dimensional finite-element method. The effective mode volume, V_m, is the ratio of a mode's total energy density per unit length to its peak energy density, where $W(r)$ is the energy density.

$$V_\text{m} = \frac{W_\text{total}}{\max[W(\mathbf{r})]} = \frac{1}{\max[W(\mathbf{r})]} \iiint W(\mathbf{r}) \text{d}^3 r \tag{S5}$$

$$W(\mathbf{r}) = \frac{1}{2}\left[\text{Re}\left(\frac{d(\omega\epsilon)}{\omega}\right)\right]|\mathbf{E}(\mathbf{r})|^2 + \mu|\mathbf{H}(\mathbf{r})|^2 \tag{S6}$$

To estimate the threshold gain of the mode, we solved the eigenmodes at an increasing imaginary part of permittivity (gain) of the perovskite. The threshold gain that compensates the absorption and radiation losses (real oscillation frequency) is approximately 3382 cm^{-1}. The other mode has a larger threshold gain and a frequency that deviates farther from the gain window of perovskite; hence, it is less likely to be the lasing mode.

Note S5. Extraction of the spontaneous-emission coupling factor.

We used the rate equations of carrier density N and photon density S to fit the light-in-versus-light-out curves of nanolasers:

$$\frac{\partial N}{\partial t} = \frac{1}{V}\frac{\eta_{p,n}P^n}{n\hbar\omega_p} - \frac{N}{\tau_{sp}} - v_g g(N)S, \tag{1a}$$

$$\frac{\partial S}{\partial t} = -\frac{S}{\tau_p} + \Gamma\beta\frac{N}{\tau_{sp}} + \Gamma v_g g(N)S, \tag{1b}$$

$$g(N) = a(N - N_{tr}), \tag{1c}$$

where V is the volume of the active region; n is the order of the pump process; $\eta_{p,n}$ is the n-photon pump coefficient; P is the pump power; $\hbar\omega_p$ is the photon energy of the pump; τ_{sp} is the spontaneous emission lifetime; v_g is the group velocity; $g(N)$ is the material gain and is modeled as a linear function of N; τ_p is the photon lifetime; Γ is the confinement factor; β is the spontaneous-emission coupling factor; a is the differential gain; and N_{tr} is the transparency density.

The pump can be a pulse train with period T and variable peak power, or a continuous-wave (CW) beam with infinite period but constant power. For a physical variable X, let us define its time average within a period T as $\bar{X}$ and apply this average to Eqs. (1a) and (1b). With $\overline{(\partial N/\partial t)} = \overline{(\partial S/\partial t)} = 0$, $\overline{P^n} = \zeta_n\bar{P}^n$ (ζ_n is a factor depending on the pulse shape and repetition rate), and the approximation $\overline{NS} \approx \bar{N}\bar{S}$, we can eliminate $\bar{N}$ and express $\bar{S}$ as a function of the mean pump power $\bar{P}$. The time-averaged observed power $\bar{P}_{obs}$ is then

$$\bar{P}_{\text{obs}} = \eta_{\text{ex}} \hbar \omega \frac{V_{\text{m}} \bar{S}}{\tau_{\text{p}}}, \tag{2}$$

where η_{ex} is the external quantum efficiency including the effects of out-coupling from the nanolaser to free space and detectability of the characterization system; $\hbar \omega$ is the photon energy of the lasing mode; and $V_{\text{m}} = V/\Gamma$ is the mode volume.

In practice, we rescale $\bar{P}_{\text{obs}}$ and $\bar{P}$ with some scaling powers $P_{\text{obs,s}}$ and P_{s}, respectively, which are chosen at one's convenience (they are not fitting parameters). After solving the time average of Eqs. (1a) and (1b), we express the scaled observed power $\bar{P}_{\text{obs}}/P_{\text{obs,s}}$ in terms of the scaled pump power $\bar{P}/P_{\text{s}}$ as

$$\frac{\bar{P}_{\text{obs}}}{P_{\text{obs,s}}} = \frac{1}{2} \left\{ \lambda_1 \left(\frac{\bar{P}}{P_{\text{s}}} \right)^{\lambda_4} - (\lambda_2 + \lambda_3) + \sqrt{\left[\lambda_1 \left(\frac{\bar{P}}{P_{\text{s}}} \right)^{\lambda_4} - (\lambda_2 + \lambda_3) \right]^2 + 4\lambda_1 \lambda_2 \left(\frac{\bar{P}}{P_{\text{s}}} \right)^{\lambda_4}} \right\}, \tag{3}$$

where parameters λ_1 to λ_4 are defined as follows:

$$\lambda_1 = \frac{\eta_{\text{ex}} \hbar \omega V_{\text{m}}}{P_{\text{obs,s}}} \left(\frac{\Gamma \zeta_n}{V} \frac{\eta_{\text{p},n} P_{\text{s}}^n}{n \hbar \omega_{\text{p}}} \right), \tag{4a}$$

$$\lambda_2 = \frac{\eta_{\text{ex}} \hbar \omega V_{\text{m}}}{P_{\text{obs,s}}} \frac{\beta}{\tau_{\text{sp}} \tau_{\text{p}} v_{\text{g}} a}, \tag{4b}$$

$$\lambda_3 = \frac{\eta_{\text{ex}} \hbar \omega V_{\text{m}}}{P_{\text{obs,s}}} \frac{(1-\beta)}{\tau_{\text{sp}} \tau_{\text{p}} v_{\text{g}} a} \left[1 + \tau_{\text{p}} \Gamma v_{\text{g}} a N_{\text{tr}} \right], \tag{4c}$$

$$\lambda_4 = n. \tag{4d}$$

At the high-pump limit, equation (3) can be approximated as

$$\frac{\bar{P}_{\text{obs}}}{P_{\text{obs,s}}} \approx \lambda_1 \left(\frac{\bar{P}}{P_{\text{s}}} \right)^{\lambda_4} - \lambda_3, \tag{5a}$$

and therefore parameter λ_3 is related to the time-average threshold pump power $\bar{P}_{\text{th}}$ at which the right-hand side of Eq. (5a) vanishes:

$$\bar{P}_{\text{th}} = P_{\text{s}} \left(\frac{\lambda_3}{\lambda_1}\right)^{1/\lambda_4}. \tag{5b}$$

We adopt the method of least-square fitting and treat parameters λ_1 to λ_4 as fitting parameters to the relation between $\log_{10}(\bar{P}_{\text{obs}}/P_{\text{obs,s}})$ and $\log_{10}(\bar{P}/P_{\text{s}})$. The reason for the logarithmic-scale fitting is to grasp the turn-on behavior of nanolasers which may appear insignificant in the linear scale. In addition, the order n of pump process is taken as a fitting parameter (λ_4) since it may deviate from the ideal number in some experimental conditions. The parameter λ_4 can be fixed if necessary. After these fitting parameters are obtained, we then estimate the spontaneous-emission coupling factor β as

$$\beta \approx \frac{\lambda_2}{\lambda_2 + \lambda_3}, \tag{6}$$

where we have further assumed that the condition $\tau_{\text{p}} \Gamma v_{\text{g}} a N_{\text{tr}} \ll 1$ holds so that the corresponding term in Eq. (4c) is dropped.

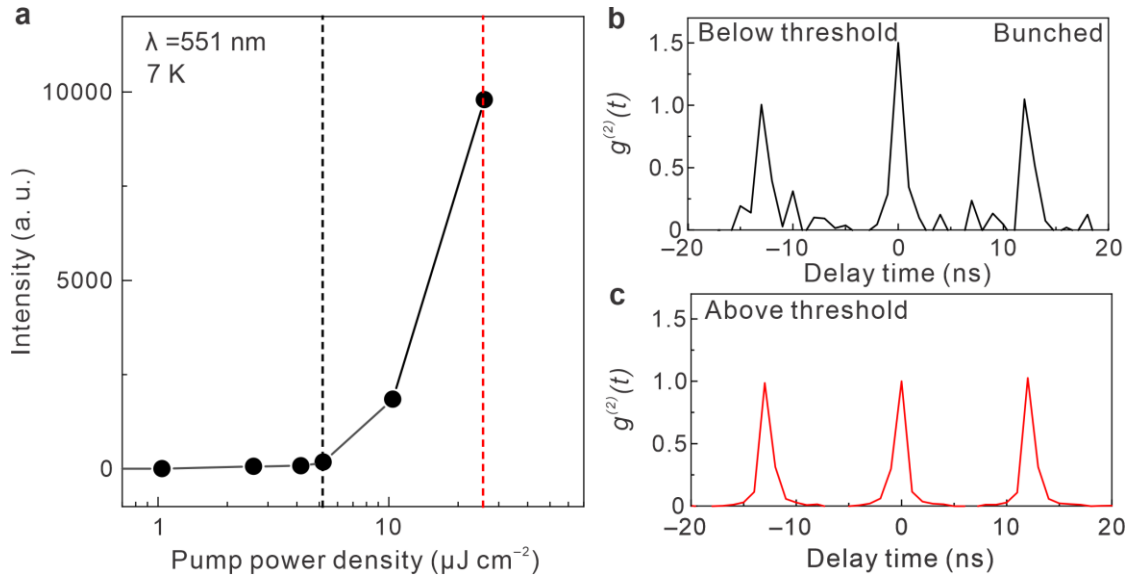**Note S6. Temporal coherence signature by second order correlation function measurements.**

Figure S5. Temporal coherence signature of the plasmonic upconverting nanolaser determined from second-order photon correlation function measurements obtained at 7 K. (a) Optical intensity versus pump fluences for the nanolasing mode at 551 nm with a lasing threshold of approximately 10 μJ cm^{-2}. The black and red dashed lines indicate the fixed pump fluence that we use below and well above the lasing threshold, respectively. (b) Below the lasing threshold (5 μJ cm^{-2}), g$^{(2)}$(t = 0) is greater than one, representing spontaneous emission (thermal bunched state). (c) Above the lasing threshold (26 μJ cm^{-2}), g$^{(2)}$(t = 0) approaches unity, which represents the temporal coherence signature of lasing. This result was obtained by using a Hanbury Brown–Twiss (HBT) setup equipped with quantum correlation analysis software (QuCou, PicoQuant).
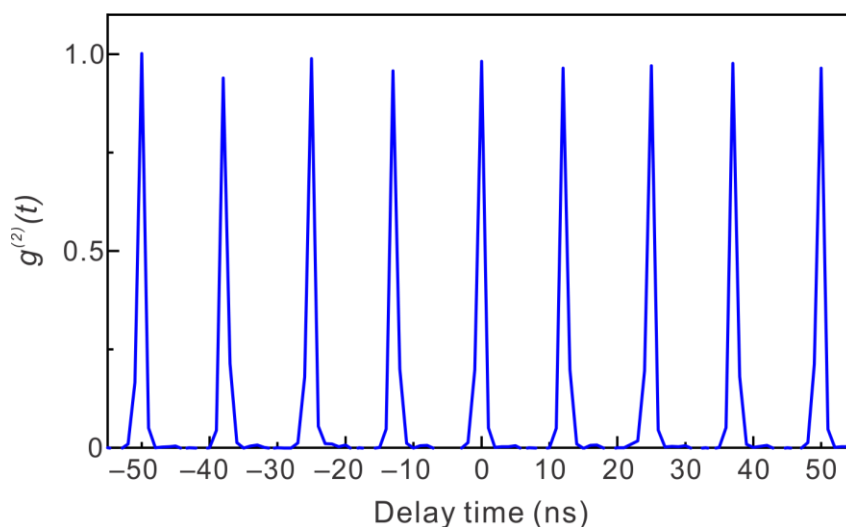
Figure S6. Second-order photon correlation function of the pulsed laser at 800 nm with an ultrafast pulsed duration of 100 fs and repetition rate of 80 MHz. This plot can be used to identify the point of zero time delay in the Hanbury Brown–Twiss system.

Supplementary References

(1) Lu, Y.-J.; Sokhoyan, R.; Cheng, W.-H.; Kafaie Shirmanesh, G.; Davoyan, A. R.; Pala, R. A.; Thyagarajan, K.; Atwater, H. A., Dynamically Controlled Purcell Enhancement of Visible Spontaneous Emission in a Gated Plasmonic Heterostructure. *Nat. Commun.* **2017,** *8*, 1631.

(2) Patsalas, P.; Kalfagiannis, N.; Kassavetis, S., Optical Properties and Plasmonic Performance of Titanium Nitride. *Mater.* **2015,** *8*, 3128.

(3) Gu, Z. Y.; Wang, K. Y.; Sun, W. Z.; Li, J. K.; Liu, S.; Song, Q. H.; Xiao, S. M., Two-Photon Pumped $CH_3NH_3PbBr_3$ Perovskite Microwire Lasers. *Adv. Opt. Mater.* **2016,** *4*, 472−479.

(4) Zhang, W.; Peng, L.; Liu, J.; Tang, A.; Hu, J. S.; Yao, J.; Zhao, Y. S., Controlling the Cavity Structures of Two-Photon-Pumped Perovskite Microlasers. *Adv. Mater.* **2016,** *28*, 4040−4046.

(5) Xu, Y.; Chen, Q.; Zhang, C.; Wang, R.; Wu, H.; Zhang, X.; Xing, G.; Yu, W. W.; Wang, X.; Zhang, Y.; Xiao, M., Two-Photon-Pumped Perovskite Semiconductor Nanocrystal Lasers. *J. Am. Chem. Soc.* **2016,** *138*, 3761−3768.

(6) Wang, X.; Zhou, H.; Yuan, S.; Zheng, W.; Jiang, Y.; Zhuang, X.; Liu, H.; Zhang, Q.; Zhu, X.; Wang, X.; Pan, A., Cesium Lead Halide Perovskite Triangular Nanorods as High-Gain Medium and Effective Cavities for Multiphoton-Pumped Lasing. *Nano Res.* **2017,** *10*, 3385−3395.

(7) Tang, X.; Hu, Z.; Yuan, W.; Hu, W.; Shao, H.; Han, D.; Zheng, J.; Hao, J.; Zang, Z.; Du, J.; Leng, Y.; Fang, L.; Zhou, M., Perovskite $CsPb_2Br_5$ Microplate Laser with Enhanced Stability and Tunable Properties. *Adv. Opt. Mater.* **2017,** *5*, 1600788.

(8) Huang, C.; Wang, K.; Yang, Z.; Jiang, L.; Liu, R.; Su, R.; Zhou, Z.-K.; Wang, X., Up-Conversion Perovskite Nanolaser with Single Mode and Low Threshold. *J. Phys. Chem. C* **2017,** *121*, 10071−10077.

(9) Wang, S.; Wang, K.; Gu, Z.; Wang, Y.; Huang, C.; Yi, N.; Xiao, S.; Song, Q., Solution-Phase Synthesis of Cesium Lead Halide Perovskite Microrods for High-Quality Microlasers and Photodetectors. *Adv. Opt. Mater.* **2017,** *5*, 1700023.

(10) Tang, B.; Sun, L.; Zheng, W.; Dong, H.; Zhao, B.; Si, Q.; Wang, X.; Jiang, X.; Pan, A.; Zhang, L., Ultrahigh Quality Upconverted Single-Mode Lasing in Cesium Lead Bromide Spherical Microcavity. *Adv. Opt. Mater.* **2018,** *6*, 1800391.

(11) Zheng, Z.; Wang, X.; Shen, Y.; Luo, Z.; Li, L.; Gan, L.; Ma, Y.; Li, H.; Pan, A.; Zhai, T., Space-Confined Synthesis of 2D All-Inorganic $CsPbI_3$ Perovskite Nanosheets for Multiphoton-Pumped Lasing. *Adv. Opt. Mater.* **2018,** *6*, 1800879.

(12) Liu, Z. Z.; Hu, Z. P.; Shi, T. C.; Du, J.; Yang, J.; Zhang, Z. Y.; Tang, X. S.; Leng, Y. X., Stable and Enhanced Frequency up-Converted Lasing from $CsPbBr_3$ Quantum Dots Embedded in Silica Sphere. *Opt. Express* **2019,** *27*, 9459−9466.

(13) Leguy, A. M. A.; Azarhoosh, P.; Alonso, M. I.; Campoy-Quiles, M.; Weber, O. J.; Yao, J.; Bryant, D.; Weller, M. T.; Nelson, J.; Walsh, A.; van Schilfgaarde, M.; Barnes, P. R. F., Experimental and Theoretical Optical Properties of Methylammonium Lead Halide Perovskites. *Nanoscale* **2016,** *8*, 6317−6327.